AD-A155 251 A STUDY OF THE CYCLICAL VARIATIONS OF CORONAL HOLES AND THEIR RELATION TO.. (U) AMERICAN SCIENCE AND ENGINEERING INC CAMBRIDGE MA SPACE SYSTE.. J M DAVIS ET AL. DEC 84 1/1

UNCLASSIFIED ASE-4928 AFGL-TR-85-0003 F19628-84-C-0037 F/G 3/2 NL

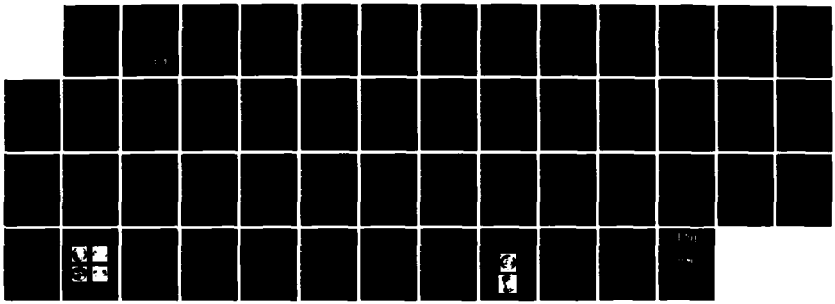

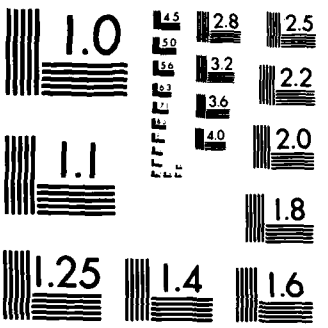

MICROCOPY RESOLUTION TEST CHART
NATIONAL BUREAU OF STANDARDS-1963-A

(2)

AFGL-TR-85-0003

A STUDY OF THE CYCLICAL VARIATIONS OF CORONAL HOLES AND THEIR RELATION TO OPEN MAGNETIC FIELDS

John M. Davis
David F. Webb

American Science and Engineering, Inc.
Space Systems Division
Fort Washington
Cambridge, Massachusetts 92139

AD-A155 251

Final Report
8 November 1983 - 30 September 1984

December 1984

Approved for public release; distribution unlimited

DTIC FILE COPY

AIR FORCE GEOPHYSICS LABORATORY
AIR FORCE SYSTEMS COMMAND
UNITED STATES AIR FORCE
HANSCOM AFB, MASSACHUSETTS 01731

DTIC
ELECTE
JUN 1 2 1985
S D
G

85 5 17 175

This report has been reviewed by the ESD Public Affairs Office (PA) and is releasable to the National Technical Information Service (NTIS).

This technical report has been reviewed and is approved for publication.

Richard C. Altrock
Contract Manager

STEPHEN L. KEIL
Branch Chief

FOR THE COMMANDER

RITA C. SAGALYN

Division Director

Qualified requestors may obtain additional copies from the Defense Technical Information Center. All others should apply to the National Technical Information Service.

If your address has changed, or if you wish to be removed from the mailing list, or if the addressee is no longer employed by your organization, please notify AFGL/DAA, Hanscom AFB, MA 01731. This will assist us in maintaining a current mailing list.

Do not return copies of this report unless contractual obligations or notices on a specific document require that it be returned.

Unclassified

SECURITY CLASSIFICATION OF THIS PAGE

REPORT DOCUMENTATION PAGE

1a. REPORT SECURITY CLASSIFICATION Unclassified	1b. RESTRICTIVE MARKINGS None
2a. SECURITY CLASSIFICATION AUTHORITY	3. DISTRIBUTION/AVAILABILITY OF REPORT Approved for public release; distribution unlimited
2b. DECLASSIFICATION/DOWNGRADING SCHEDULE	
4. PERFORMING ORGANIZATION REPORT NUMBER(S) ASE-4928	5. MONITORING ORGANIZATION REPORT NUMBER(S) AFGL-TR-85-0003
6a. NAME OF PERFORMING ORGANIZATION American Science and Engineering, Inc. 6b. OFFICE SYMBOL (If applicable) AS&E	7a. NAME OF MONITORING ORGANIZATION Air Force Geophysics Laboratory
6c. ADDRESS (City, State and ZIP Code) Space Systems Division Fort Washington Cambridge, MA 02139	7b. ADDRESS (City, State and ZIP Code) Hanscom AFB, MA 01731
8a. NAME OF FUNDING/SPONSORING ORGANIZATION 8b. OFFICE SYMBOL (If applicable)	9. PROCUREMENT INSTRUMENT IDENTIFICATION NUMBER F19628-84-C-0037
8c. ADDRESS (City, State and ZIP Code)	10. SOURCE OF FUNDING NOS. PROGRAM ELEMENT NO. 61102F; PROJECT NO. 2311; TASK NO. G3; WORK UNIT NO. CW
11. TITLE (Include Security Classification) A Study of the Cyclical Variations of Coronal Holes and Their Relation To Open Magnetic Fields	
12. PERSONAL AUTHOR(S) John M. Davis and David F. Webb	
13a. TYPE OF REPORT Final Report 13b. TIME COVERED FROM 11/8/83 TO 9/30/84	14. DATE OF REPORT (Yr., Mo., Day) December 1984 15. PAGE COUNT 51
16. SUPPLEMENTARY NOTATION	
17. COSATI CODES FIELD / GROUP / SUB. GR.	18. SUBJECT TERMS (Continue on reverse if necessary and identify by block number) Coronal Holes, Solar Cycle Variations, Solar X-Ray, Coronal Images,
19. ABSTRACT (Continue on reverse if necessary and identify by block number) (See Over)	
20. DISTRIBUTION/AVAILABILITY OF ABSTRACT UNCLASSIFIED/UNLIMITED X ☐ SAME AS RPT. ☐ DTIC USERS ☐	21. ABSTRACT SECURITY CLASSIFICATION Unclassified
22a. NAME OF RESPONSIBLE INDIVIDUAL Richard C. Altrock	22b. TELEPHONE NUMBER (Include Area Code) 22c. OFFICE SYMBOL PHS

Accession For
NTIS GRA&I ☒
DTIC TAB ☐
Unannounced ☐
Justification
By
Distribution/
Availability Codes
Dist | Avail and/or Special
A/1

DD FORM 1473, 83 APR EDITION OF 1 JAN 73 IS OBSOLETE

Unclassified

SECURITY CLASSIFICATION OF THIS PAGE

This contract was a study of possible variations in the observed flux from coronal holes over a solar cycle and their relationship to solar magnetic fields. The variation of X-ray emission from coronal holes was measured and compared with data on photospheric magnetic field strength and models of open field structures from holes. The data set consisted of reduced X-ray images from AS&E rocket flights and digitized photospheric magnetic field strength data from Mt. Wilson and Kitt Peak observatories over the period 1974 to 1981.

The results are as follows. We found that soft X-ray emission from coronal holes could be detected in the rocket data, confirming earlier Skylab results. Also, this emission appeared to vary systematically over an 8-year period, from a minimum in mid-1974 to a maximum about one year after sunspot activity maximum. This conclusion is strengthened by three other observations: (1) HeI 10830 A coronal holes exhibited decreased contrast during this same period; (2) the particular holes that we measured were typical of those at each phase of the cycle in terms of their evolutionary and interplanetary characteristics; and (3) the X-ray hole emission followed a similar trend in Harvey et al.'s (1982) data whereby the photospheric field strength of near-equatorial holes increased systematically by a factor of three between 1975 and 1980. Further, our own measurements of field strengths within the X-ray hole boundaries were sparse but generally in agreement with the Harvey et al. trend.

TABLE OF CONTENTS

FOREWORD

This document is the final report for AFGL Contract Number F19628-84-C-0037. The period of performance on the contract was from 8 November 1983 to 30 September 1984, as extended by Modification No. P00001 dated 5 October 1984. The scientific objectives and statement of work for the contract were described in AS&E's unsolicited proposal ASE-4777, dated 24 January 1983.

The contract was for the study of possible variations in the observed flux from coronal holes over a solar cycle and their relationship to solar magnetic fields. Included in the study was the investigation of the variation of X-ray emission from coronal holes over a solar cycle and the comparison of these data with the photospheric magnetic field flux and models of open field structures from holes. The data set consisted of reduced X-ray images from AS&E rocket flights and digitized, ground-based photospheric magnetic field data. The Principal Investigator on the contract was Dr. John M. Davis. The data reduction, calibration and subsequent analyses were performed primarily by David F. Webb.

1.0 INTRODUCTION

Studies during the last decade and a half and including the Skylab era have shown the importance of low-latitude coronal holes as sources of high speed solar wind streams (Krieger et al., 1973; Nolte et al., 1976; Zirker, 1977; Sheeley and Harvey, 1978; 1981). Potential magnetic field calculations have been used to identify regions of open field lines from observed photospheric line-of-sight fields (Altschuler and Newkirk, 1969; Levine, 1977, 1982). During the declining phase of the last solar cycle (the Skylab period), a nearly one-to-one association between coronal holes and open fields was established (Zirker, 1977). However, it has been suggested that this relation is less clear during other parts of the cycle. For instance, Levine (1977; 1982) showed that during Skylab and around solar maximum open fields also emanate from active regions, and Nolte et al. (1977) and Sheeley and Harvey (1978; 1981) showed that during solar minimum and the rise to maximum there were solar wind sources (presumably connected with the corona by open field lines) that could not be identified with low-latitude coronal holes.

Coronal holes were first and most easily identified in soft X-ray and XUV images as regions of very low brightness in comparison to surrounding active regions or other large-scale, closed structures. However, since such observations have not been available routinely since the end of the Skylab mission, an alternative method for determining positions and sizes of coronal holes has been employed using ground-based HeI 10830 A data. The 10830 A images have been used extensively (e.g., Sheeley and Harvey, 1978; 1981) for determining coronal hole positions and areas and their relationships to solar wind speeds and geomagnetic activity indices.

Rocket flights subsequent to the Skylab mission have provided us with high resolution, full-disk solar X-ray images at approximately 18-month intervals over the present solar cycle. Recently at AS&E we began a study using these images to advance our understanding of coronal holes in three ways:

1. To test the agreement between X-ray and 10830 A images for determining coronal hole boundaries,

2. To examine possible variations in the characteristics of coronal holes occurring over the solar cycle,

3. By comparison with potential field models to evaluate the correspondence between coronal holes and open field configurations.

The first phase of this program was performed in collaboration with J.W. Harvey of the National Solar Observatory (NSO) (Kahler et al., 1983). Significant differences were found to exist between coronal hole boundaries determined in the 10830 A and X-ray images. This in turn implies that the use of the 10830 A data for detailed inferences of coronal hole parameters such as area must be viewed with caution.

In examining coronal holes in the AS&E X-ray and Kitt Peak 10830 A images, Kahler et al. (1983) found what appeared to be a decrease in the brightness contrast between the coronal holes and large-scale coronal structure after the 1973-1974 period. Such a "weakening" of holes was also observed in the 10830 A data alone during 1976-1977 by Sheeley and Harvey (1978). Also, Levine (1982) determined that the association between predicted open magnetic structures and 10830 A coronal holes was less clear after the Skylab period. Specifically, he found frequent examples of open magnetic structures which were associated with small holes that were 'faint' or 'weak' in HeI 10830 A, i.e., having less contrast to their surroundings than the larger holes of the declining phase of the cycle. Finally, Harvey et al. (1982) found that low latitude coronal holes contained three times more flux near sunspot maximum than near minimum even though their areas were comparable. Taken together, these results suggest that over the solar cycle the distinction in terms of open and closed fields between the coronal holes and large-scale structure is not as clear as during the declining phase of the last solar cycle.

The purpose of the present study was to pursue the second and third phases of our overall program discussed above to use the solar X-ray images to study coronal holes and open fields over the solar cycle. Our specific approach was to try and answer three questions relating to cyclical variations in coronal holes and open fields:

1. In the light of ambiguous quantitative results using Skylab X-ray data, is X-ray emission from coronal holes detectable above background, and, if so, does it vary over the cycle?

2. Can a change in the plasma conditions within low contrast holes explain the difference in visibility, and can they in turn be related to the increased photospheric field strength found in the holes of the new cycle?

3. Do X-ray coronal holes correspond to open field regions at all stages of the cycle?

The ultimate goal of this program is to develop a model for the variation of conditions within coronal holes over a solar cycle and to relate this model to the propagation of the solar wind.

We were unable to address all three of these questions in this study because of difficulties in cross-calibrating the X-ray data, which consumed much of the project time. However, we were able to answer the first question in the affirmative and to make considerable progress toward our understanding of the second.

In the next section we describe the observational analysis in terms of our approach, data selection, the analysis of the X-ray images, the analysis of the magnetic flux, and comparison of the two data sets over the cycle. A summary of the results and conclusions in the light of present coronal hole models are discussed in Section 3. Tables and figures highlight the salient results.

2.0 OBSERVATIONAL ANALYSIS

2.1 Approach

The overall scientific objective of this study was to use coronal hole measurements of soft X-ray coronal flux and photospheric magnetic field strength to examine possible variations in these parameters over a solar cycle with the goal of improving our understanding of the physics of coronal holes. Our approach involved three phases. First, we wanted to select the best images from among seven AS&E rocket flights from 1974 through 1981 to be calibrated and reduced to arrays of energy flux at the focal plane. Specifically, the average energy flux within the coronal hole boundaries determined by Kahler et al. (1983) would be measured to enable possible variations in the emission from holes over the cycle to be examined. Second, using the technique of Harvey et al. (1982), we would use Kitt Peak synoptic maps of average magnetic field strength within the X-ray coronal hole boundaries to compare with the X-ray flux measurements. Where necessary, the synoptic maps would be complemented by daily Kitt Peak maps or daily and synoptic maps from Mt. Wilson Observatory. Finally, the results of the analyses and comparison would be interpreted in terms of models of coronal hole formation and structure and of cyclical variations of open field structures as predicted by potential field models.

During the study this approach had to be modified in the following ways. Only X-ray images obtained with polypropylene (PP) and beryllium (BE) filters and with the fused silica (glass) mirror payload were analyzed. This simplified the data reduction, minimized interflight calibration problems, and permitted us to ignore the effects of scattering in the coronal hole flux measurements. In addition, we decided not to analyze the November 1979 data for various reasons (discussed later). Kitt Peak synoptic magnetic maps were unavailable for all of the rocket periods. These data were supplemented by printouts of Mt. Wilson daily maps. Mt. Wilson synoptic maps and Kitt Peak daily maps were not used. Although the two formats differed in sensitivity and spatial and temporal averaging, large-scale averaging and intercomparisons of the two sets for two dates gave us confidence that the differences were not important. Finally, rectangular dark subareas within each coronal hole rather than the entire

coronal hole area were used to determine the net average X-ray flux and field strength for each hole.

2.2 Data Selection

Since the Skylab period full-disk soft X-ray images of the solar corona have been obtained on seven AS&E rocket flights. Table I lists the dates, times and pertinent instrumental data for each of these flights. Kahler et al. (1983) provides more details on the X-ray instrumentation of the flights, except for the 17 November 1976 flight. They did not analyze the data from that flight because of the lack of HeI data, whereas we included it in our analysis. We excluded the 16 September 1976 and 16 November 1979 data because they were obtained with the Kanigen (metal) mirror. That mirror is less efficient and has substantially greater scattering than the glass mirror (see Davis et al., 1977 for a comparison). No measurable coronal holes were visible on the 16 November 1979 images, but small low to mid-latitude holes were visible on 7 November 1979 (see Figure 4 in Webb et al., 1984) However, we could not use the data from that flight because scattered radiation from a flare in the southeast precluded photometric measurements in faint areas.

Therefore, images from four rocket flights remained to be reduced for our study. The PP filters chosen for these flights were similar to Filter 3 used with the Skylab S-054 instrument (Vaiana et al., 1977) to study coronal holes. The PP image exposure times, exposure ratios and filter thicknesses used in our calibrations are given in the last three columns of Table I.

PP images from the four flights are shown in Figure 1 and the X-ray coronal hole boundaries from Kahler et al. (1983) are reproduced in Figure 2 to the same scale as Figure 1. The 17 November 1976 boundaries, though not included in their paper, were drawn by Kahler et al. during their analysis. Their 1976 and 1981 boundaries compare favorably with those determined independently by Nolte et al. (1977) and Webb et al. (1984), respectively. Solar north is up and east to the left in all of the figures in this report.

We wanted to compare as a function of time the X-ray emission with the magnetic flux density from the coronal holes, using the boundaries determined by Kahler

et al. We used a variation of the technique of Harvey et al. (1982) to compare the X-ray and photospheric magnetic data. Their technique was to transfer HeI 10830 A coronal hole boundaries to synoptic magnetic flux maps constructed for each Carrington rotation. These maps are routinely available from Kitt Peak in digital form as described by Harvey et al. (1980). However, as Table II shows, the Kitt Peak synoptic maps were not available for long periods around the dates of the first two rocket flights due to weather or instrumental problems. Also, a three-day data gap centered on 31 January 1978 degraded the synoptic Kitt Peak data for that flight. Therefore, we obtained daily averaged magnetic flux maps from Mt. Wilson Observatory for the dates and times shown in Table II. Thus, the Mt. Wilson data became the primary source of comparison with the X-ray coronal emission.

2.3 Analysis of the X-Ray Data

2.3.1 Background

In order to determine coronal plasma parameters, the X-ray density images must be calibrated and reduced to arrays of energy flux deposited on the film plane. For our purpose determining the net average energy flux within coronal holes, and to a limited extent within restricted areas of the diffuse coronal background, was the end result of the X-ray analysis. So we did not determine electron temperatures, densities or emission measures within the holes although these parameters could, in principle, be derived from the energy flux.

Except for the mirror, the rocket images were obtained with the same film emulsion (SO-212) and similar instrumental parameters used with the AS&E Skylab telescope. Thus, we had hoped to be able to closely follow calibration procedures used for the Skylab data and described in Vaiana et al. (1977). Fundamental to these procedures is knowledge of the conversion of SO-212 film density to energy flux at certain wavelengths determined by laboratory measurements. Such measurements on film sensistrips exposed with aluminum (8.3 A) and carbon (44.7 A) X-ray sources were made for analysis of both Skylab and rocket images obtained with the beryllium and polypropylene filters, respectively. However, during the Skylab analysis problems were found especially with the 44 A calibration data (e.g., Maxson and Vaiana, 1977). Kahler (1982) first noted

that large discrepancies also existed in the post-Skylab rocket calibration data, and that these were not due to film development chemistry. We confirmed that, with the possible exception of the November 1976 data, the 44 A rocket data were inadequate for our calibration. To overcome this problem we used synthesized calibration data based on the image data themselves to provide absolute energy calibrations for each flight. This procedure follows that of Maxson and Vaiana (1977) which they developed to analyze areas of low film density and is appropriate for coronal hole data. However, it was more time consuming and limited the scope of our overall analysis. Because of the uncertainties of the film calibration, the final coronal hole energy flux values had relatively large error ranges. However, we feel that this analysis is the best that could be achieved with this set of data and that it provides meaningful limits on the cyclical dependence of energy flux from coronal holes.

Each flight image was scanned with AS&E's PDS microdensitometer to produce a digitized density array with 20 micron pixels, equivalent to 2.8 arc-sec spatial resolution. Before proceeding with the data reduction, we had to be confident that emission from coronal holes could be detected in the rocket data. As a preliminary check on the detectability and variability of such X-ray emission, we analyzed the density data in terms of histograms of spatial frequency vs. gross PDS density. We found that the full-disk average density of each image, normalized and corrected to an equivalent Skylab long exposure, supported our impression from the photographs (Kahler et al., 1983) that the distribution of coronal emission changes systematically with the cycle. For instance, the full-disk averaged coronal density obtained from a 1974 PP rocket image was similar to an equivalent Skylab exposure (Maxson and Vaiana); the full-disk density was lower in 1976 near sunspot minimum and highest in 1981 just after sunspot maximum.

The histograms reveal that coronal holes are detectable above background in terms of density alone, even in the June 1974 images near sunspot minimum. Figure 3 shows full-disk histograms for the first two rocket flights. Plotted is the frequency of digitized density (PDS) in terms of 3 x 3 averaged pixels uncorrected for background level, scattering or exposure differences. Small-area histograms within the large coronal hole on 27 June 1974 reveal that the hole emission peaks at about 40 PDS units, or 30 with background sub-

tracted. Thus, the hole emits above background, at a value which is slightly less than that measured in Skylab CH 1 (Maxson and Vaiana). On 17 November 1976 the hole emission arose from the large north and south polar holes and the equatorial extension from the south pole (Figure 1). This emission comprises the first peak and tail in the 1976 histogram. These plots also reveal the distribution of specific large-scale coronal features on each image and how this distribution changes with the cycle. As Maxson and Vaiana showed for Skylab, the diffuse large-scale structure (LSS) is the dominant contributor to the non-flaring X-ray flux. In broadband images the LSS usually appears in these plots as the dominant peak with typical values above 100 PDS units. The June 1974 image illustrates well the major coronal components that were visible in the Skylab data one half to one year earlier. The vertical lines indicate the characteristic densities of the film background, the large coronal hole, diffuse LSS, brighter LSS and active regions. These distributions changed dramatically during the solar cycle as evidenced by the sharp change between mid-1974 and late 1976, near solar minimum when the corona was dominated by the diffuse emission (Figure 3).

Details of the calibration and reduction procedures used in the analysis of the X-ray images are contained in the Appendix. In the next section are summarized the results of the X-ray analysis.

2.3.2 Results of the X-Ray Analysis

Listed in Table III and plotted in Figure 4 are the net average X-ray intensities and their uncertainties derived for the coronal hole subareas shown in Figure 2. These subareas were chosen to encompass areas of minimal brightness in the holes; i.e., regions obviously brighter than the hole base level and film defects were avoided. These coronal hole subareas are indicated on Figure 2 by the boxes labelled 'c'; the box sizes and shapes are only approximate. Generally the average gross density and statistical error at at least two locations per hole and on two adjacent PP images was measured.

Figure 4 is assembled in time order on a semi-log plot. (Note that the abcissa is not drawn to scale.) Plotted at the left are the only three sets of published Skylab X-ray measurements of the emission from coronal holes. These

data were all obtained with the S-054 instrument on SO-212 film. The first two sets are measurements of two areas in Coronal Hole 1 (CH 1) made in August 1973 using two toe calibration methods (Maxson and Vaiana). The third set consists of three measurements of the emission from CH 6 shortly after its birth on the disk in October 1973 (Solodyna et al., 1977). Measurements from the four rocket data sets follow in time order from left to right. A clear trend in the data is apparent, with the hole measurements in 1973, 1974 and 1976 being similar and very low, rising to maximum values in 1981. Examining only the rocket data, the hole emission was at its lowest in June 1974, a factor of 3 higher in November 1976 near solar minimum and a factor of 8 higher in January 1978. The emission from the large southern hole in February 1981 near solar maximum was an order of magnitude higher than in 1978, but with large uncertainties due to large differences between the rocket and Skylab film calibrations and possible scattering contributions.

At this point a comment is needed on the existence of X-ray emission from holes with regard to the contribution of scattering to the measurements. Some controversy arose concerning the Skylab measurements of coronal hole emission. Maxson and Vaiana concluded that CH 1 had significant emission. They made no corrections for scattering, but claimed that such effects were minimized in their data because they chose subareas far from bright sources, CH 1 had a large area and cross sections through the hole revealed flat-bottomed profiles inconsistent with scattering effects. On the contrary, Solodyna et al. estimated significant scattering contributions from individual sources and so corrected the measured CH 6 emission. However, unlike CH 1, CH 6 at the time of Solodyna et al.'s measurement was a very small hole surrounded by LSS and active regions, and flaring occurred in a limb region during some of the observations. They concluded that the X-ray hole emission after its development "was consistent with zero within our assessment of the experimental uncertanties."

Like Maxson and Vaiana we chose to make no scattering corrections to the rocket data, but we also attempted to minimize such effects by choosing subareas away from bright regions and checking cross-sectional profiles through the holes. In addition, we used the shortest exposures which still showed hole boundaries, and used only rocket data that was obtained with the glass mirror. Scattering from this mirror is substantially reduced compared with the Skylab metal mir-

ror, especially at shorter wavelengths, and the scattering is nearly wavelength independent (Davis and Krieger, 1982). Both the Skylab and rocket measurements were made with data obtained on the same film emulsion and with similar PP filters.

It must be emphasized that neither the Skylab nor our coronal hole measurements include the effects of possible systematic errors arising from such factors as poorly known uncertainties in the calibration data and the absolute source spectrum. Specifically, in our analysis systematic errors due to our ignorance of the wavelength dependence of film aging, of the temperature dependence of areas of low film density, and of the details of any scattering contribution could be present. Nevertheless, we believe that our conservative approach to the cross-calibration of the rocket data has minimized the effects of such errors; the relative trend of the X-ray measurements, especially, should not be effected by systematic errors.

We conclude that the rocket data confirms Maxson and Vaiana's view that detectable X-ray emission arises from coronal holes and our data reveal that this emission appears to increase as the cycle evolves from activity minimum to maximum. One can take the view that despite the diversity in hole area, location on the disk and evolutionary characteristics, and possibly calibration procedures, the four independent data sets from 1973 to 1976 reveal remarkably consistent X-ray hole emission values varying over this period by only about a factor of three. The 1974 rocket measurements are also consistent with Solodyna et al.'s measurements of CH 6 made only 8 months earlier.

Finally, listed in Table IV and plotted in Figure 5 are the net average intensities and uncertainties derived for the diffuse coronal background subareas shown in Figure 2 and labeled 'Q.' These subareas were chosen to include large-scale areas of minimal coronal emission on the disk away from coronal holes, active regions and bright LSS. Such areas form part of the "background" coronal emission and are likely associated with diffuse loops anchored in the network fields. This emission is typically at the faint end of the class of large-scale structures (LSS) discussed by Maxson and Vaiana and others. LSS are associated with large, more clearly defined loops often forming arcades over neutral lines (McIntosh et al., 1976). One might expect the diffuse emis-

sion to remain relatively constant over the cycle, especially if there are no great temperature variations in the plasma. Table IV and Figure 5, which are in the same format as the coronal hole data, reveal more consistency among the data, but the same general trend as seen in the coronal hole data. Plotted on the left for reference are Maxson and Vaiana's values for two LSS areas during Skylab.

2.4 Analysis of the Photospheric Magnetic Field Strength Data

The selection and acquisition of the photospheric magnetic field data for our study were discussed in Section 2.2. Table II lists the dates and times of the Mt. Wilson magnetograms and the availability of the Kitt Peak synoptic maps that we analyzed.

The Mt. Wilson daily maps were our primary source of magnetic field data because they were available on or within one day of each of the four rocket flights analyzed. We desired one map on the day of the flight and one each on the day before and the day after in order to minimize any day to day variations in the maps. However, for the 1978 flight only maps on the day of the flight and the day after were available, and in 1981 only one map was available on the day after the flight. Fortunately, good Kitt Peak data were obtained for this flight.

The daily Mt. Wilson data were provided to us in the form of computer printouts of averages in 34 x 34 equal intervals of sine longitude (central meridian distance) and sine latitude. Therefore, the spatial resolution of an average pixel at sun center was about 2-1/2°, steadily degrading toward the limb. Thus these represented large area averages of flux density or field strength in units of Gauss. The magnetograph measures the longitudinal component of the photospheric field in the 5250 A line of FeI. Because of weakening in this line, the values measured are on the order of a factor of two too low, but this effect varies across the disk (Howard and Stenflo, 1972). Our measurements were corrected for the effects of line weakening and foreshortening as described below.

The Kitt Peak synoptic maps are available for each Carrington rotation and are described in detail by Harvey et al. (1980). We obtained computer printouts of equal-area pixels of one degree longitude by (1/90) unit of sine latitude of the mean field strength in Gauss. The observations used here were obtained with the 512-channel magnetograph which measures the longitudinal field in the 8688 A line of FeI. This line saturates in umbral regions but requires no correction elsewhere. The values are accurate to about $\pm$ 1 G (J. Harvey, private communication). Where necessary a cosine weighting function in longitude has been applied to the synoptic data to merge it across daily data gaps. The data used for the 1978 comparison was effected by a 3-day data gap centered on 31 January 1978, the day of the rocket flight.

Both formats were treated similarly except that many more points went into averaging of the Kitt Peak arrays, increasing their statistical weight. (But no formal error analysis was applied to any of the magnetic data.) We selected rectangular subareas on the magnetic maps which would correspond spatially to the coronal hole subareas in which the X-ray measurements were made. The magnetic map areas were determined from drawings of the X-ray hole boundaries using Stoneyhurst grids to get the heliographic coordinates of the chosen box. The subareas in which the magnetic flux was measured are shown by the dashed outlines on Figure 2. For the 1976 and 1981 data these areas were made to coincide approximately with the X-ray subareas. For the 1974 and 1978 data, we were able to use single large subareas to increase the statistical accuracy of the measurements.

The results of our analysis of the photospheric field strength in coronal holes are listed in Table V. The table lists the date and subarea measured by the same hole designation used for the X-ray measurements in Table III. Column 3 gives the known polarity of the hole as determined by H-alpha synoptic charts in Solar-Geophysical Data and the magnetic field/solar wind observations of Sheeley and Harvey (1981). Column 6 contains the average measured longitudinal field strength, B_m, in Gauss measured for each hole subarea. These were obtained by simply computing the algebraic sum of all pixels within the chosen subarea and dividing by the number of subarea pixels. With one exception the measured polarities agree with the expected ones. That exception was the measurement of the north polar hole on 17 November 1976. The net polarity was

negative, not positive, but of very low flux and the measurement may have been effected by foreshortening near the limb.

We made the assumption that the observed fields are radial and performed a first order correction for the projection effect of the measured field of the form $B_c = B_m/\cos \theta$, where θ is the great-circle distance from sun center to the subarea. These corrected values, B_c, are listed in Column 7. The value of θ is listed in the last column. For the Mt. Wilson data θ was taken to be the great circle distance to the center of the subarea. This arc was calculated according to the formula $\sin (90 - \theta) = \cos a \cos b$, where a and b are solar latitude and CMD. This average distance was found to be nearly equal to that determine by performing the calculation pixel by pixel. As noted earlier, a correction for line weakening is required for the Mt. Wilson data. We applied a correction of the form given by Howard (1977) to derive the "true" field strength, B_T;

$$B_T = B_m \left(\frac{0.48 + 1.33 \cos \theta}{\cos \theta} \right)$$

This value is listed in Column 8 of Table V. In addition, the June 1974 Mt. Wilson measurements were increased by 20% to account for a change in the magnetograph aperture in 1975 (R. Howard, private communication). The Kitt Peak synoptic data are already corrected for the longitude projection effect, so we applied the cosine correction in latitude only. The Kitt Peak values for θ_c are estimates only and are placed in parentheses.

The average flux values from Table V (B_T for Mt. Wilson and B_c for Kitt Peak) are plotted in Figure 6 by date. Measurements limbward of about $\theta = 60°$ are placed in parentheses indicating that they should be assigned lower weight. Mt. Wilson observations not obtained on the day of the flight are indicated by the symbol 'x'. Comparison of the Kitt Peak synoptic and Mt. Wilson daily measurements in January 1978 and February 1981 indicate no clear pattern between the two FeI line measurements. However, the 1978 and 1981 subarea No. 1 measurements were at an average distance from sun center > 60° and therefore subject to considerable foreshortening. Therefore, for comparison we have only the single average measurement within the 1981 hole equatorial extension (θ 40°). (Although the Mt. Wilson map was obtained a day later, the hole was then

nearly at CMP.) The corrected Mt. Wilson and Kitt Peak values agree remarkably well, within 3%, giving us confidence that our magnetic field measurements are reasonably consistent.

Harvey et al. (1982) used Kitt Peak synoptic images to measure the magnetic fluxes and field strengths in 33 10830 A coronal holes from 1975 to 1980. They measured no holes beyond a latitude of 50° and made no corrections for projection effects. In Figure 7a we have plotted all of their data on field strengths given in their Table I in the same format as our magnetic data. The lines join measurements close in time to guide the eye. This plot illustrates their result that during this part of the solar cycle, lower latitude holes contained three times more flux near activity maximum than at minimum. There appears to be a steadily rising trend to the data.

In addition, on Figure 7a we have plotted our average Mt. Wilson measurements as crosses to ascertain how the fluxes from our holes matched those of Harvey et al. (1982) over the same period. We averaged together the corrected measurements for the three days centered on the rocket flights of 27 June 1974 and 17 November 1976. We included the average of the Mt. Wilson measurements on 31 January and 1 February 1978 even though θ exceeded 60° and the values differed by a factor of 3. Finally, the single Mt. Wilson measurement on 14 February 1981 was on the day after the rocket flight. One of the Harvey et al. measurements, that of their hole No. 18 on 19 October 1976, was of the same southern equatorial extension that we measured on 16-18 November 1976. Our averaged measurement for this hole of -3.42 G agrees favorably with their value of -2.7 G. In general, our hole flux values follow the trend of the Harvey et al. data with the possible exception of the 1978 value. The 1981 value lies below their trend, but our measurement was made after the end of their study.

2.5 Comparison of the X-Ray and Magnetic Fluxes in Coronal Holes

Figure 8 provides a direct comparison of the solar corona observed in soft X-rays on 13 February 1981 (left) with Kitt Peak and Mt. Wilson magnetograms of the 13th and 14th (middle and right), respectively. The X-ray image was obtained about one year after the sunspot maximum of the current cycle. The large asymmetric, high-latitude coronal hole we studied was part of the first

new-cycle polarity (+) region which had expanded from its birth as a small, mid-latitude hole 10 rotations earlier on CR 1695 (Webb et al., 1984). In Figure 10 the X-ray boundary of the hole has been superposed on the magnetograms. We can see that the hole boundary encloses an area on both images of unipolar (positive), moderately strong field which has been found to be a characteristic of such holes over at least one solar cycle.

Figures 4 and 7 provide the primary basis of comparison between the X-ray flux and the photospheric magnetic field strength from the coronal holes we studied. Although the X-ray data consist of snapshots of one hemisphere of the sun at only four times (or five including the November 1979 period) durirg the cycle, they sampled key dates during the declining phase of the last cycle (1974), at solar minimum (1976), mid-way up the rising part of Cycle 21 (1978), and around solar maximum (1979 and 1981). It is of interest to place our data in the context of the more continuous studies since Skylab involving HeI holes and the magnetic field (Sheeley et al., 1976; Sheeley and Harvey, 1978, 1981; Harvey et al., 1982; Levine, 1982; and Webb et al., 1984).

For each flight all the X-ray measurements in Table III have been averaged together and plotted as a single value in Figure 7b. The X-ray hole measurements show an increasing trend with the cycle in general agreement with the magnetic flux (Figure 7a), but with a much greater increase, two orders of magnitude, from 1974 to 1981. If we exclude the 1981 data because of its larger uncertainties, the increase between 1974 and 1978 is still large -- about one order of magnitude.

3.0 CONCLUSIONS

This study was part of a general program at AS&E to utilize soft X-ray images of the solar corona to investigate the characteristics of coronal holes over the solar cycle. We now summarize our observational results in the light of the three questions posed in the Introduction.

The first question can now be answered in the affirmative. We conclude that the rocket results confirm earlier Skylab results, though these were interpreted in different ways, that net soft X-ray emission from coronal holes is detectable. With the possible exception of the February 1981 data, the energy fluxes we measured were consistent with the Skylab results despite the fact that the Skylab and rocket telescopes, essentially the optics, were different from each other.

The second part of Question 1 can also be answered in the affirmative. Within the context of our limited data set, the observed X-ray coronal hole emission does appear to vary in a systematic way over an 8-year period of the solar cycle. Comparison of 21 measurements made in 9 coronal hole areas between August 1973 and November 1976 reveal small but measurable energy fluxes within about a factor of 3 of each other. The general trend of the measurements is sinusoidal, with minimum flux at the latter period just before sunspot minimum, then increasing flux through 1981, about one year after sunspot maximum. We cannot rule out that the coronal hole emission for October 1973 (Skylab) and June 1974 (rocket) was below the detection threshold and therefore that these values are upper limits.

For each flight we also made measurements of the diffuse background coronal emission as a way of calibrating the coronal hole flux variations against overall variations in solar plasma conditions. These results are presented in Figure 5. Overall there is a similar tendency for the diffuse emission to increase with the cycle. However, the relative increase is less than for the coronal hole emission. From 1974 to 1981 the diffuse emission increased by an order of magnitude and between 1974 and 1978 by a factor of 3; the equivalent increases in hole emission over the same intervals were factors of 100 and 10, respectively. Also, on 27 June 1974 the diffuse emission appeared to be de-

pressed in the lane separating the north polar hole from its large equatorial extension. If we compare only the northwest diffuse subarea No. 3 with the subareas in 1976 and 1978, the measurements all fall within the error bars (albeit large) and are reasonably consistent with Maxson and Vaiana's Skylab measurements of LSS. Thus, our photometric results support the qualitative suggestions of Kahler et al. (1983) and Sheeley and Harvey (1978; 1981) that the brightness contrast between coronal holes and large-scale structure decreased during this period of the rise to activity maximum.

By themselves these limited X-ray results do not provide compelling evidence for a solar cycle variation in overall coronal hole emission. But when combined with the qualitative, but more frequent observations of a "weakening" or decreased contrast of 10830 A holes and an increase in the surface magnetic flux within holes over the same period, this conclusion is strengthened.

In addressing our second question, the magnetic field data support a relationship between increasing X-ray hole emission and increasing field strength over this same period of the cycle. This support comes primarily from the data of Harvey et al. (1982 - our Figure 7b) which show an increase by a factor of three in the field strength of near-equatorial coronal holes between 1975 and 1980. Our direct measurements of the field strength within the X-ray hole boundaries fit the overall trend of the Harvey et al. data but are too sparse to conclude much else. The January/February 1978 magnetic field data don't follow the trend of increasing X-ray hole emission, although the magnetic data are effected by foreshortening and, of course, any given coronal hole might have anamolous properties. The February 1981 magnetic fluxes are the highest in agreement with the X-ray results, but still below the trend of the Harvey et al. data.

At this point it is useful to discuss the particular coronal holes that we measured in the context of their evolutionary and interplanetary characteristics to assure ourselves that these holes are not atypical. We will confine our discussion to those holes or extensions of holes which occurred on or near the equator, since the correlation of such holes with the solar wind is known to be high.

The large June 1974 hole was the only one in our data which extended over the equatorial region. This hole evolved from a separate, small equatorial hole during Skylab (CH 4) to join with its like-polarity north polar hole by mid-January 1974 (Solodyna et al., 1975). As shown in the Bartels display of Sheeley and Harvey (1978; 1981) intercomparing coronal holes, solar wind speed, the IMF and the C9 geomagnetic index, by June 1974 this hole was about midway through its lifetime. Through mid-1975 this hole and another of opposite polarity formed a two-sector structure of strong, recurrent solar wind structure. These holes, and the wind streams, had a 27-day recurrence period. All these characteristics were typical of equatorial holes observed during Skylab (e.g., Zirker, 1977).

The other coronal holes we measured were either in the polar regions or were equatorward extensions from large polar or high-latitude holes. The polar cap holes in 1974 and 1976 were typical of the near-solar minimum part of the cycle (Hundhausen et al., 1981).

The negative-polarity, equatorial extension measured on 17 November 1976 was the early development of a long-lived (about 9 rotations), but weak 10830 A hole discussed by Sheeley and Harvey (1978, their Figure 4). The evolution of this feature was influenced by the growth of a new-cycle (positive polarity) BMR which weakened it. As Sheeley and Harvey noted, "Despite its weak appearance, this hole was associated with one of the most prominent recurrence patterns of high-speed solar wind and enhanced geomagnetic activity that occurred during 1976-1977." The hole was typical of this period in having a higher synodic rotation period (28 days) than during the decline of the previous cycle.

This pattern was mimicked by the January 1978 south polar extension hole. Our observation occurred during the early development of this long-lived, rapidly rotating (29-day period) region, which was part of a region which persisted for nearly two years (Sheeley and Harvey, 1981)! We have already discussed the February 1981 southern hole, which was also long-lived, of new-cycle polarity and may have been associated with a recurrent wind stream.

In every case, including that of the "weak" November 1976 hole, the X-ray near-equatorial holes were associated with IMF polarity of the same sign (Harvey and

Sheeley, 1981). This fact and the correlation between recurrent patterns of high speed wind and geomagnetic activity suggest that these holes were strongly connected with the interplanetary medium flow by open field lines emanating from the base of the holes.

We were unable to further investigate this inference for our data by directly comparing the location of the holes with regions of open fields as deduced, say, from potential field models. Levine has made such comparisons with the Skylab data (e.g., Levine, 1977) and more recently with 10830 A holes observed in 1975 and 1978-1979 (Levine, 1982). In the context of this study, his comparisons were made during two periods (March to November 1975 and May 1978 to March 1979) during which we had no rocket observations.

However, in the case of the 1978-1979 period, we can compare Levine's (1982) study of open fields with our observation of the southern hole in January 1978. As we noted above, this hole was associated with a long-lived, recurrent hole and wind pattern. This hole persisted in 10830 A throughout the second period of Levine's study. His Figures 3-6 confirm that this lobe extending from the south polar region was detected as a strong open field region of similar size and shape and persisting through the period of Levine's study.

Therefore, with respect to our Question 3, we suggest that open field regions in general corresponded to the X-ray coronal holes we observed during this phase of the cycle. Unfortunately, direct support for this supposition is lacking. We could only infer this association for the 1978 coronal hole, and open field calculations are presently lacking for the times of the other flights. Indirect, but strong support for the supposition also comes from the good correlation between the hole locations and timing, and interplanetary medium parameters. There appears to be a moderate correlation between the field strength in holes and the X-ray energy flux over the cycle, but the variation of X-ray flux in holes does not seem to be strongly dependent on the degree of open field structure. We hope eventually to extend our study to include a direct comparison of the X-ray hole data with open field structure as deduced from potential field calculations.

4.0 ACKNOWLEDGEMENTS

We would like to thank J. Harvey and R. Howard of the National Solar Observatory for providing the photospheric magnetic field data and for helpful discussions concerning its use. We also acknowledge useful discussions on calibration of the X-ray data with C. Maxson of the Center for Astrophysics and S. Kahler of Emmanuel College. We appreciate the assistance of M. Rizza and F. Simpson in the preparation of the figures.

5.0 REFERENCES

Altschuler, M.D. and Newkirk, G., Jr.: 1969, Solar Phys. 46, 185.

Davis, J.M. and Krieger, A.S.: 1982, Solar Phys. 80, 295.

Davis, J.M., Golub, I. and Krieger, A.S.: 1977, Astrophys. J. 214, L141.

Harvey, J., Gillespie, B., Miedaner, P. and Slaughter, C.: 1980, Report UAG-77, World Data Center A, NOAA, Boulder, CO.

Harvey, K.L., Sheeley, N.R., Jr., and Harvey, J.W.: 1982, Solar Phys. 79, 149.

Howard, R.: 1977, Solar Phys. 52, 243.

Howard, R. and Stenflo, J.O.: 1972, Solar Phys. 22, 402.

Hundhausen, A.J., Hansen, R.T. and Hansen, S.F.: 1981, J. Geophys. Rev. 86, 2079.

Kahler, S.W.: 1982, internal AS&E memo.

Kahler, S.W., Davis, J.M. and Harvey, J.W.: 1983, Solar Phys. 87, 47.

Krieger, A.S., Timothy, A.F. and Roelof, E.C.: 1973, Solar Phys. 29, 505.

Levine, R.H.: 1977 in J.B. Zirker (ed.) Coronal Holes and High Speed Wind Streams, Colorado Associated University Press, Boulder, CO, p. 103.

Levine, R.H.: 1982, Solar Phys. 79, 203.

Maxson, C.W. and Vaiana, G.S.: 1977, Astrophys. J. 215, 919.

McIntosh, P.S., Krieger, A.S., Nolte, J.T. and Vaiana, G.: 1976, Solar Phys. 49, 57.

Nolte, J.T. Krieger, A.S., Timothy, A.F., Gold, R.E., Roelof, E.C., Vaiana, G.S., Lazarus, A.J., Sullivan, J.D. and McIntosh, P.S.: 1976, Solar Phys. 46, 303.

Nolte, J.T., Davis, J.M., Gerassimenko, M., Lazarus, A.J. and Sullivan, J.D.: 1977, Geophys. Res. Lett. 4, 291.

Sheeley, N.R., Jr., and Harvey, J.W.: 1978, Solar Phys. 59, 159.

Sheeley, N.R., Jr., and Harvey, J.W.: 1981, Solar Phys. 70, 237.

Sheeley, N.R., Jr., Harvey, J.W. and Feldman, W.C.: 1976, Solar Phys. 49, 271.

Simon, R., Haggerty, R., Golub, I., Krieger, A.S., Silk, J.K., Timothy, A.F. and Vaiana, G.S.: 1975, "Response of Photographic Film to Soft X-Ray Radiation," AS&E Document ASE-3775.

Solodyna, C.V., Nolte, J.T. and Krieger, A.S.: 1975, memo to Skylab Solar Workshop Participants.

Solodyna, C.V., Krieger, A.S. and Nolte, J.T.: 1977, Solar Phys. 54, 123.

Tucker, W.H. and Koren, M.: 1971, Astrophys. J. 168, 283; Erratum, 170, 621.

Vaiana, G.S., VanSpeybroeck, L., Zombeck, M.V., Krieger, A.S., Silk, J.K. and Timothy, A.: 1977, Space Sci. Instru. 3, 19.

Webb, D.F., Davis, J.M. and McIntosh, P.S.: 1984, Solar Phys. 92, 109.

Zirker, J.B. (ed.): 1977, Coronal Holes and High Speed Wind Streams, Colorado Associated University Press, Boulder, CO.

APPENDIX: CALIBRATION AND REDUCTION OF THE X-RAY DATA

In this section we summarize our procedures for calibrating and reducing the X-ray data, highlighting those aspects whereby our procedure differed from the standard one (e.g., Vaiana et al., 1977). The standard procedure for converting the digitized density arrays to arrays of energy flux involves use of density-to-energy (D to E) calibration curves and corrections for the film base density, chemical fogging, radiation fogging and scattering due to the mirrors. For the rocket analysis we ignored any correction for radiation fogging, because of the short duration (5 min) of each flight, and scattering (see Section 2.3.2).

In the soft X-ray region we have found that the net density can be related to the power per unit area by means of the semi-empirical relationship:

$$D = f(D_{max}, \gamma, (a\lambda) Ft)$$

where D_{max} = maximum possible net density

γ = slope of the linear portion of the D to E curve

a = film speed which is inversely proportional to the energy at zero density

F = Power per unit area of the exposure

t = exposure time

D_{max} and t are obtained experimentally; γ and $a\lambda$ are wavelength-dependent and therefore temperature-dependent parameters and must be determined via laboratory calibrations and/or from the data itself. For our analysis we determined γ iteratively using the "scatter plot" method (Vaiana et al., 1977) on two active regions per flight for two adjacent PP exposures. D is a function of the product $(a\lambda)E$; at a given temperature $a\lambda$ is a constant for any flight and at this stage is usually set = 1 and determined later.

Film Speed Calibration

Two major problems of the X-ray analysis which consumed much of our time were the estimation of $a_\lambda(T)$ for each flight and the calibration of areas of low film

density. a_μ cannot be determined from image data, and there is no theoretical model for its behavior in the X-ray region. Our knowledge of its behavior is based entirely on laboratory measurements (Simon, 1975). However, the 44.7 A sensistrips developed with each flight film load were inadequate for calibration use and the 8.3 A data suggested the possibility that the SO-212 film had significantly aged since the early 1970's when our stock was purchased from Kodak. For example, as expected with aging, the film contrast (γ) and speed (a_μ) tended to decrease with time resulting in more deposited energy being required to expose the film grains to a given density, However, this tendency at 8.3 A was not entirely systematic and we have no information on how the aging process would affect the wavelength dependence of a_μ. There was no evidence of aging in the visible light sensistrips. Therefore, we decided on a fairly conservative approach, which was to determine a range of a_μ, and therefore a range of energy flux, for each flight by using at one extreme the best Skylab experimental fit of $a_\mu(\lambda)$ and at the other a fit with the same slope as Skylab but with an offset "pinned" to the 8.3 A value of a_μ for a particular flight. These $a_\mu(\lambda)$ fits are shown in Figure 9. An exception was the 17 November 1976 data where both the rocket 8.3 and 44.7 A and Skylab sensistrip data were used to determine the range of $a_\mu(\lambda)$.

The approximate ranges of $\gamma(T)$ and $a_\mu(T)$ could be determined for each flight. To do this one must know the relationship between the solar coronal emission and the flux imaged by the telescope at Earth. We followed closely the procedure discussed by Vaiana et al. (1977). Briefly, the total irradiance at the focal plane reduces to the equation:

$$E_i = \frac{A}{4\pi f^2} \iint N_e^2(\xi)\, P(\lambda, T(\xi))\, T_i(\lambda)\, d\lambda\, d\xi,$$

where E_i has units of erg $cm^{-2}s^{-1}$, i denotes the filter used, $T_i(\lambda)$ is the filter function, and the integration is along the line of sight. If the plasma is isothermal, the quantity $(A/4\pi f^2)$ and the emission measure, $\int N_e^2(\xi)d\xi$, are constant and the irradiance ratio in two filters, in our case PP and BF, is:

$$\frac{E_{PP}}{E_{BE}} = \frac{F_{PP}(T)}{F_{BE}(T)} = R(T)$$

where $F_i(T) = \int P(\lambda,T)\, T_i(\lambda)d\lambda$ and R is a function of temperature only.

At AS&E $P(\cdot,T)$, the spectral distribution of solar soft X-ray emission, is determined from a modified version of the Tucker and Koren (1971) theoretical spectrum. The quantity $F_i(T)$ is determined for each filter function, permitting the temperature to be determined by comparing the measured and theoretical irradiance ratios. Now in practice this procedure is modified to account for the $a_i(T)$ dependence of the filter, so that

$$R(T) = \frac{\int_{PP} \cdot a_{PP}(T)}{\int_{BE} \cdot a_{BE}(T)} \Big/ \frac{\int_{PP} \cdot a_{PP}(T)}{\int_{BE} \cdot a_{BE}(T)}$$

and we define a new quantity, Q:

$$Q = \frac{\int_{PP}}{\int_{BE}} = R(T) \frac{a_{PP}(T)}{a_{BE}(T)}$$

or

$$Q = \frac{\int_{PP}(T)\, a_{PP}(T)}{\int_{BE}(T)\, a_{BE}(T)}$$

For a given feature Q is determined from the incident irradiance ratio and $F_i(T)$ from the theoretical filtered spectrum weighted by the appropriate $a_{\mu i}(T)$ dependence (Figure 9). In our analysis we determined the range of a_μ for each flight by deriving for two active region areas the appropriate D to E conversion (and γ), the ratio Q and therefore the temperature range, and finally the a_μ range over this temperature for both of the $a_\mu(\cdot)$ fits.

Low Density Calibration

The second major problem faced in our analysis was how to properly calibrate data of low density, such as the emission from coronal holes and the diffuse background. One of the major disadvantages of film as a detector is that its energy response is nonlinear. The standard model discussed above for density to energy conversion in the X-ray regime applies only to the "linear" region of the X-ray characteristic curve where film density is proportional to the log of the deposited energy. Fainter than this, in the so-called "toe" region, no analyti-

cal model has been developed to describe the X-ray D to E behavior. Techniques for analyzing Skylab S-054 data in the toe region were developed by and discussed in the Appendix of Maxson and Vaiana (1977). We used their technique of using the data themselves to provide the shape of the D to E curve in the toe region, and then pinning the toe and linear regions through crossover points determined from laboratory calibration data.

Like Maxson and Vaiana, for each flight we selected coaligned areas on PP density arrays of adjacent exposures that included the coronal hole of interest and were large enough to include a sufficient number of points to adequately determine the shape of the D to E curve from near the background to the linear region. A necessary assumption of this method is that there be no significant variation in temperature over the field, so the D to E area must be restricted. This toe density calibration curve can then be converted to an "absolute" D to E curve by pinning it at crossover points, which are assumed to be absolutely calibrated, and extrapolating down from these points using the known exposure ratios. The PP exposures and their exposure ratios used for the toe calibrations and coronal hole analyses for each flight are given in columns 6 and 7 of Table I.

The crossover pinning points were determined in the following way. The linear regions of calibrated (corrected γ's) D to E curves for both filters for two active regions were shifted along the energy axis so as to bracket the extremes of the $a_{\mu}(T)$ fits assumed appropriate for that flight. This resulted in a family of curves determined by the number of curves of different slope and the a_{μ} ranges. The minimum number of curves would be 8; i.e., if the two active regions had the same average temperature, then there would be one PP and one BE curve which each would be shifted to bracket the ranges of $a_{\mu}(T)$ determined for that filtered spectrum. In practice the range of a_{μ} for the two active regions might overlap and the range of $a_{\mu_{BE}}(T)$ was usually small and could be approximated by a single curve. Points where the BE and PP curves cross are presumed to have the correct D to E values since the absolute calibration should be independent of wavelength. These points, of course, are only as "absolute" as our assumptions about $a_{\mu}(T)$, which are ultimately based on the laboratory measurements. A number of crossover points result because we have used two different $a_{\mu}(T)$ fits and determined a range of a_{μ} based on these fits and a range of temper-

atures. Taking only those crossover points which allow extrapolation down into the toe region of our density calibration curves, we can then plot a family of "synthesized" D to F calibration curves for the toe region. For a given flight we need plot only the curves which yield the extreme energy limits for a given density value.

As an example Figure 10 shows the final toe calibration curves for the 27 June 1974 data. Each curve is adjusted to asymptotically approach the film background density at near-zero energy. To the left are plotted the average gross densities and statistical error bars of the central coronal hole subarea measured on the two PP images. The lower and upper limits of the equivalent net energy are read off the two curves at the given density value (crosses). Each energy value must be divided by the appropriate exposure time to yield net intensity, or focal plane energy flux in erg cm^{-2} s^{-1}. For a given density the average net intensity is the midpoint of the range and the "error bar" is 1/2 the difference between the two intensity limits.

TABLE I

AS&E Solar X-Ray Rocket Flights

Date	Carr. Rot.	CR	Time (UT)	Mirror Type	PP Exposures (sec)	N	PP Filter Thickness*
1974, June 27	1616	6	1948	Glass	19.7, 59.2	3.0	1 μm + 3500 A Al
1976, Sept. 16	1646	30	1803	Kanigen	--	--	--
1976, Nov. 17	1648	2	1827	Glass	3.7, 16.5	4.5	1 μm + 3300 A Al
1978, Jan. 31	1664	16	1841	Glass	2.6, 8.7	3.3	1 μm + 3500 A Al
1979, Nov. 7	1688	24	2053	Glass	--	--	--
1979, Nov. 16	1688	1/3	1703	Kanigen	--	--	--
1981, Feb. 13	1705	17	1916	Glass	2.8, 9.6	3.4	1 μm + 3200 A Al

* The PP filters nominally contained 1 μm of polypropylene (PP) (C_3H_6) coated with 1500 A of aluminum. All X-ray exposures are made through a 1500 A Al heat-rejection prefilter. These thicknesses can vary slightly from flight to flight.

TABLE II

Selected X-Ray Images and Magnetograms

X-Ray Images	Carr. Rot.	CR	Kitt Peak Synoptic Maps	Mt. Wilson Daily Maps*
1974, June 27, 1948	1616	6	No	June 26, 1456 27, 1652 28, 1715
1976, Nov. 17, 1827	1648	32	No	Nov. 16, 1659 17, 2243 18, 1751
1978, Jan. 31, 1841	1664	16	Yes (gap)	Jan. 31, Feb. 1, 1846
1981, Feb. 13, 1916	1705	41	Yes	Feb. 14, 2326

*Times are UT at the midpoint of the mapping interval.

TABLE III

X-Ray Energy Flux in Coronal Holes

Date	Coronal Hole Designation	PP Exposure time (s.)	Average PDS Density	Net Intensity (erg cm^{-2} s^{-1})
27 Jun 1974	1: Central	19.7	21.6 ± 1.2	0.0022 ± 0.0008
		59.2	32.6 ± 2.2	0.0021 ± 0.0007
	2: Northwest	19.7	19.5 ± 0.8	0.0017 ± 0.0013
		59.2	27.8 ± 1.9	0.0014 ± 0.0005
	2: North Polar Hole	19.7	21.05 ± 2.1	0.0021 ± 0.00155
		59.2	30.3 ± 4.1	0.0018 ± 0.0012
17 November 1976	1: Equatorial Extension	3.7	13.0 ± 0.7	0.0075 ± 0.0033
		16.5	18.8 ± 1.2	0.0056 ± 0.0020
	2: South Polar Hole	3.7	12.65 ± 0.8	0.0064 ± 0.0030
		16.5	17.4 ± 1.1	0.0046 ± 0.0017
	3: North Polar Hole	3.7	13.5 ± 0.8*	0.0083 ± 0.00385*
		16.5	19.7 ± 1.3	0.0061 ± 0.0022
31 January 1978	1: Towards Center	2.6	18.6 ± 0.9	0.0167 ± 0.0091
		8.7	25.8 ± 1.3	0.0156 ± 0.0091
	2: Towards Limb	2.6	18.1 ± 1.0	0.0156 ± 0.0084
		8.7	25.4 ± 0.8	0.01505 ± 0.0088
13 February 1981	1: Towards Limb	2.8	24.3 ± 1.4	0.1525 ± 0.1161
		9.6	39.2 ± 1.6	0.1318 ± 0.1036
	2: Towards Center	2.8	26.6 ± 1.7	0.1776 ± 0.1334
		9.6	41.8 ± 1.5	0.1525 ± 0.1195

* Value is slightly high because of film scratches.

TABLE IV

X-Ray Energy Flux in Diffuse Background Corona

Date	Background Designation	PP Exposure time (s.)	Average PDS Density	Net Intensity (erg cm^{-2} s^{-1})
27 June 1974	1: North-Central Part of CH	19.7	36.3 ± 3.2	0.0083 ± 0.0025
		59.2	58.9 ± 4.3	0.0078 ± 0.0021
	2: East Part of CH	19.7	42.7 ± 4.1	0.0115 ± 0.0032
		59.2	70.1 ± 5.8	0.0120 ± 0.00365
	3: Northwest	19.7	55.2 ± 8.5	0.0207 ± 0.0055
		59.7	89.5 ± 11.3	0.0211 ± 0.00665
17 November 1976	1: Southeast	3.7	21.5 ± 3.1	0.0327 ± 0.0116
		16.5	44.4 ± 6.2	0.03545 ± 0.0130
	2: North	3.7	21.7 ± 2.8	0.0350 ± 0.0123
		16.5	44.6 ± 5.1	0.0359 ± 0.0132
31 January 1978	1: North edge of CH	8.7	35.5 ± 3.0	0.0340 ± 0.0190
	2: Central Band	8.7	45.1 ± 4.0	0.0551 ± 0.0303
13 February 1981	1: Northeast	2.8	44.2 ± 4.9	0.5724 ± 0.4311
		9.6	77.6 ± 8.1	0.5565 ± 0.4372
	2: Center	2.8	35.05 ± 2.8	0.3429 ± 0.2578
		9.6	59.9 ± 4.8	0.3494 ± 0.2782

TABLE V

Net Magnetic Field Strength in Coronal Holes

Date	Coronal Hole Designation	Polarity	Observatory	Meas. Type	Net B_m (G)	Net B_c (G)	Net B_T (G)	θ_c (deg)
[illegible]	1,2: Central	+	MW	Daily	+1.31	+1.55	+2.87	14.5
[illegible]	1,2: Central	+	MW	Daily	+1.39	+1.79	+3.06	~19
[illegible]	1,2: Central	+	MW	Daily	+1.27	+1.79	+2.88	31.5
[illegible]	1	-	MW	Daily	-1.34	-1.51	-2.51	27.6
[illegible]	1	-	MW	Daily	-1.70 to -2.41	-2.07 to -2.93	-2.67 to -3.79	34.8
[illegible]	2	-	MW	Daily	-1.61	-3.20	-3.68	59.8
[illegible]	3	+	MW	Daily	-0.15	-0.30	-0.34	59.8
[illegible]	1	-	MW	Daily	-2.26	-3.17	-4.53	44.5
[illegible]	Southwest	-	KP	Synoptic	-0.84	-1.285	--	(55)
[illegible]	Southwest	-	MW	Daily	-0.91	-2.125	-2.23	64.6
[illegible]	Southwest	-	MW	Daily	-0.305	-0.83	-0.80	68.4
[illegible]	1	+	KP	Synoptic	+0.84	+1.55	--	(58)
[illegible]	2	+	KP	Synoptic	+4.33	+5.60	--	(40)
[illegible]	1	+	MW	Daily	+1.78	+4.45	+4.50	66.4
[illegible]	2	+	MW	Daily	+2.93	+3.83	+5.74	40.1

FIGURE CAPTIONS

Figure 1 Soft X-ray images of the solar corona for the four dates analyzed in this study. All images were obtained with the AS&E glass mirror rocket payload and with polypropylene filters. The exposure times vary. Solar north is up and east to the left for all images. The central meridian longitudes, L_o, for the four images in time order were: 237°, 220°, 175°, and 298°.

Figure 2 Tracings of X-ray coronal hole boundaries from Kahler et al. (1983) to the same scale as Figure 1. Hatched areas indicate uncertain X-ray holes. See Kahler et al. for details on how the boundaries were determined. The solid boxes indicate the subareas where the X-ray measurements of emission from coronal holes ('C') and the diffuse background corona ('Q') were made. The dashed subareas indicate where the magnetic flux was measured.

Figure 3 Full-disk histograms of spatial frequency vs. gross PDS density for the 59 sec PP exposure on 27 June 1974 (left and the 16 sec PP exposure on 17 November 1976 (right). These two images are reproduced in Figure 1. Note the change in the ordinate scales.

Figure 4 Net X-ray intensities in coronal holes averaged over the subareas indicated by the boxes labelled 'C' on Figure 2 and listed in Table III. The first three data sets are Skylab S-054 measurements of holes. The points in parentheses for November 1976 are uncertain because the average hole densities for the 3.7 sec exposure are close to the film background density.

Figure 5 Net X-ray intensities in the diffuse coronal background subareas indicated by the boxes labelled 'Q' in Figure 2 and listed in Table IV. The first two data sets are Skylab measurements of LSS areas.

Figure 6 Linear plot of corrected magnetic field strengths averaged over the subareas indicated by the dashed boxes on Figure 2 and listed in Table V. The data sets are arranged in time order to compare our measurements with those of Harvey et al. in Figure 9a. Circled points are Mt. Wilson daily data on the day of the rocket flight, and X's are such data one day before or after the flight. Squares indicate measurements from Kitt Peak synoptic maps. The parentheses indicate measurements limbward of an average $\theta = 60°$.

Figure 7 Overall comparison of the magnetic field strength and X-ray flux of coronal holes from 1974 to 1981.

(a) Semi-log plot of magnetic field strengths from Kitt Peak synoptic maps averaged over 10830 A coronal hole boundaries from 1975 to 1980. Points joined by a vertical line represent measurements of different holes made during the same months. We have plotted these data from Table I of Harvey et al. (1982); see their paper for details. The crosses indicate our averaged Mt. Wilson measurements for equatorward holes only (see text).

(b) Semi-log plot to the same time scale as (a) of the X-ray energy fluxes of the coronal holes listed in Table III. For each flight all of the measurements have been averaged together and plotted as a single point. Each error bar is a simple average of the measurement uncertainties for each flight.

Figure 8 Comparison of the solar X-ray corona observed with AS&E's rocket flight on 13 February 1981 and ground-based, photospheric magnetograms from Kitt Peak on the 13th (center) and Mt. Wilson on the 14th (right). The Mt. Wilson map is from Solar-Geophysical Data. Positive-polarity fields are indicated by white areas on the Kitt Peak image and solid lines on the Mt. Wilson map. The X-ray boundary of the large southern coronal hole has been superposed on each of the magnetograms. For the Mt. Wilson map the X-ray boundary has been adjusted to account for solar rotation.

Figure 9 Fits of the SO-212 film speed parameter, $a\mu$, as a function of X-ray wavelength. The fits are of the form $\ln a\mu = \lambda - a/b$. Circled points indicate measured data. The Skylab (S-054) and 17 November 1976 rocket fits are based on laboratory data at at least two wavelengths with $a = 14.0$, $b = 33.8$ and $a = 12.9$, $b = 47.0$, respectively. The S-054 data are from an AS&E memo by M. Gerassimenko dated 1 August 1975. The other fits are derived by "pinning" the curve with the same slope as the S-054 data to the 8.3 A value measured for each rocket flight. The values of a for those flights are: 1974: -2.0, 1978: -0.7, 1979: 31.2, and 1981: 44.3.

Figure 10 Synthesized film density to deposited energy calibration curves for the 27 June 1974 data. These curves are for the "toe" region. The shape of the curve is derived from image data and is "pinned" in absolute energy at a point that is dependent on assumptions about the fit of $a\mu(\lambda)$ and the range of temperature. The curve yielding the highest energies is pinned at the circled value: $D_{PDS} = 111$, $E = 2.7$ erg cm^{-2}; the curve yielding the lowest energies is pinned at a point beyond the scale of the graph: $D_{PDS} = 199$, $E = 8.4$. The film background density was 11 PDS units.

CORONAL X-RAY OBSERVATIONS
1974 - 1981

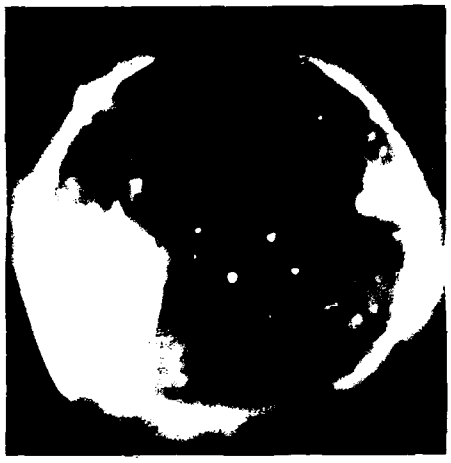

27 JUNE 1974

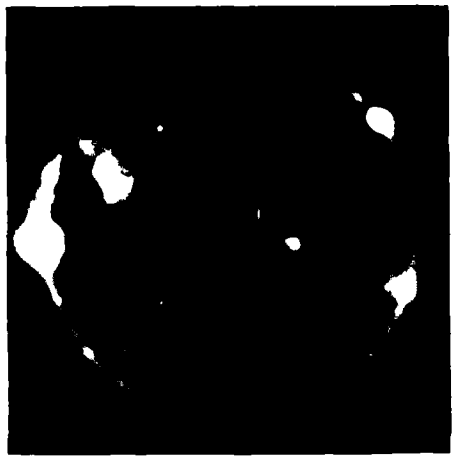

17 NOVEMBER 1976

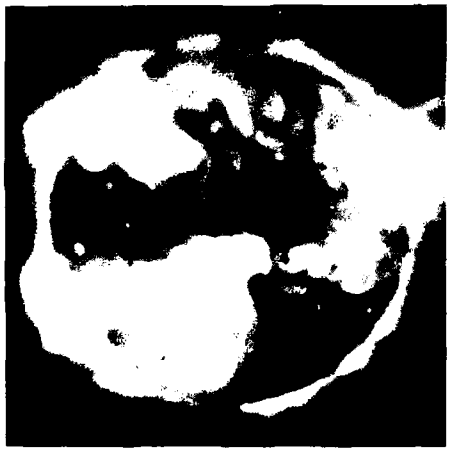

31 JANUARY 1978

13 FEBRUARY 1981

Figure A1

CORONAL HOLE BOUNDARIES

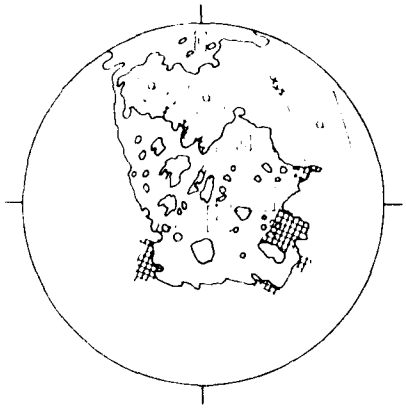

27 JUNE 1974

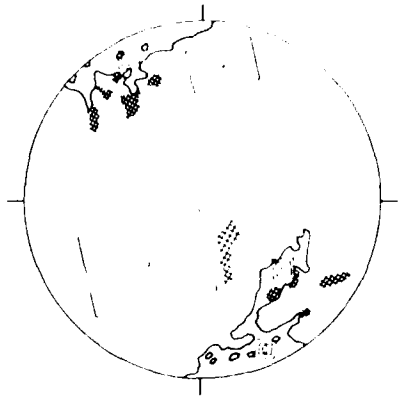

17 NOVEMBER 1976

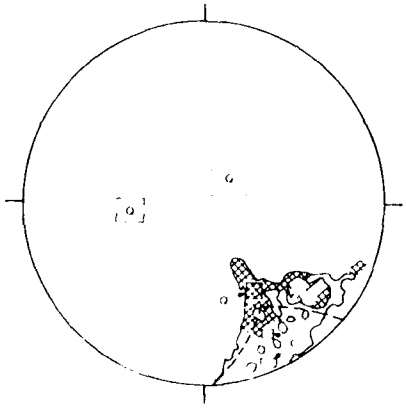

31 JANUARY 1978

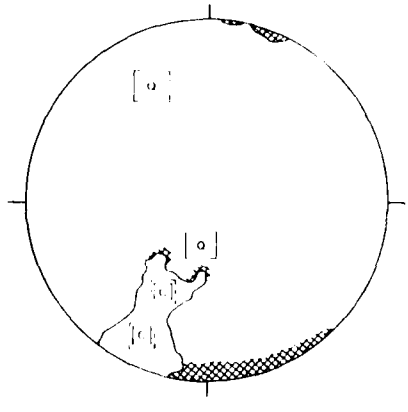

13 FEBRUARY 1981

Figure A2

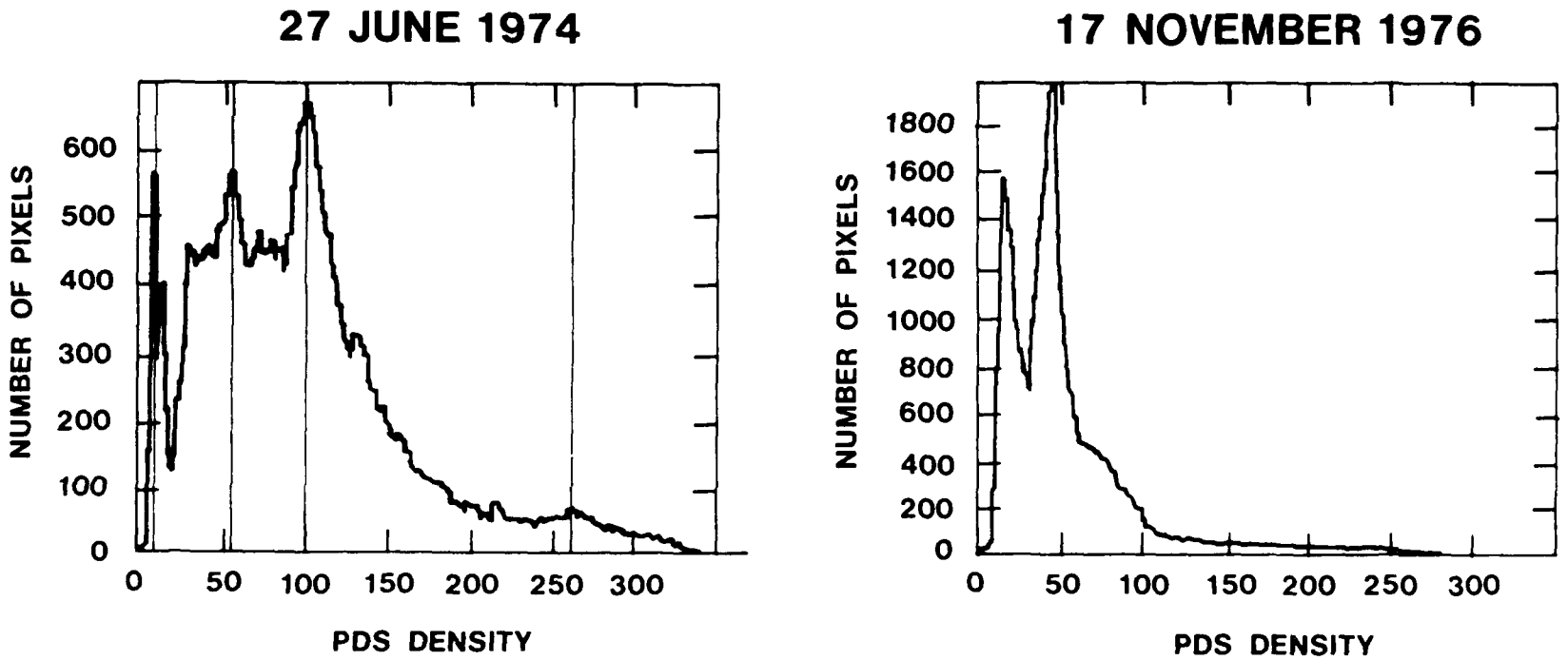
27 JUNE 1974
NUMBER OF PIXELS
0
100
200
300
400
500
600
0
50
100
150
200
250
300
PDS DENSITY
17 NOVEMBER 1976
NUMBER OF PIXELS
0
200
400
600
800
1000
1200
1400
1600
1800
0
50
100
150
200
250
300
PDS DENSITY

Figure A3

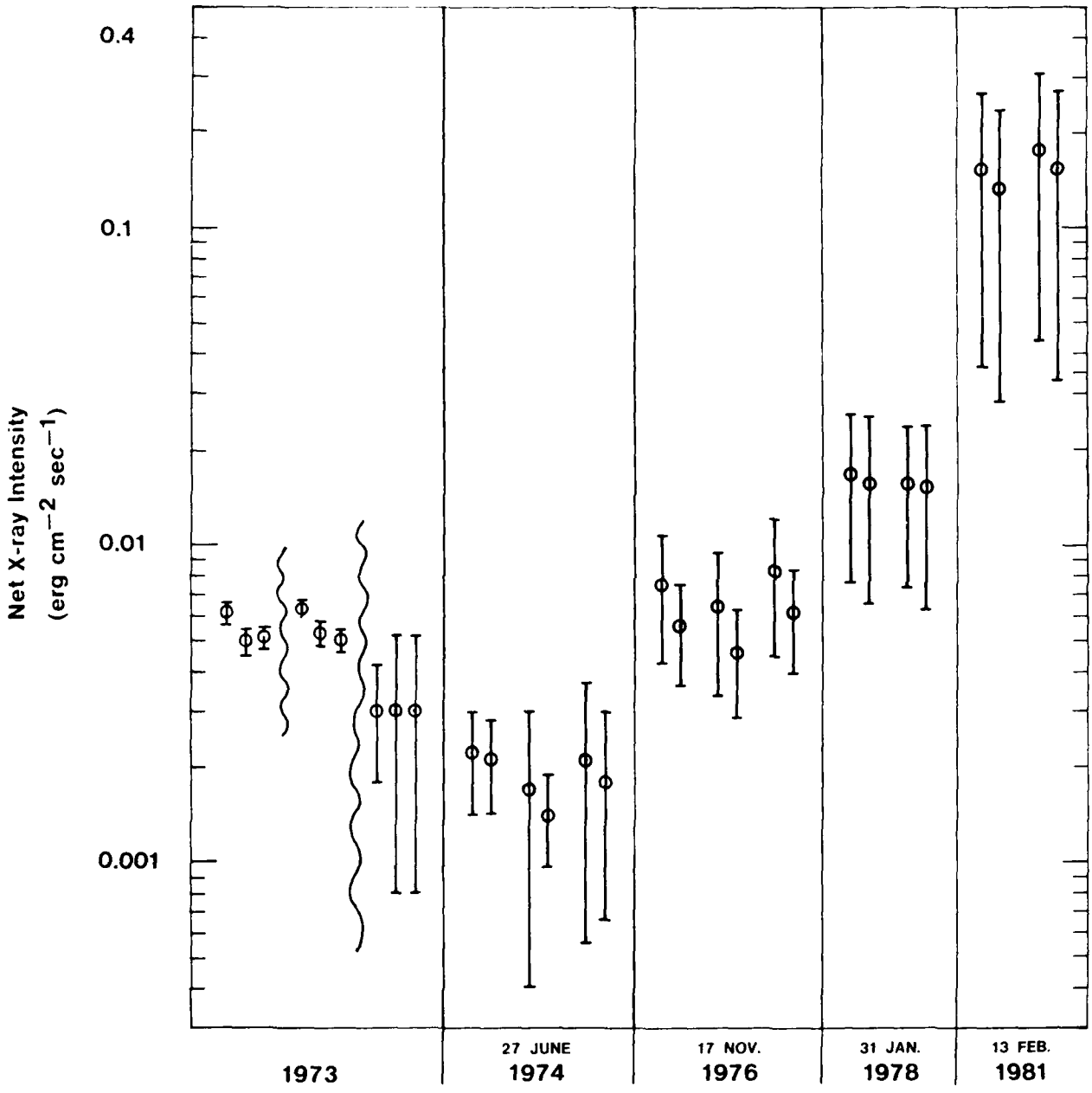
0.4
0.1
0.01
0.001
Net X-ray Intensity
(erg cm^{-2} sec^{-1})
1973
27 JUNE
1974
17 NOV.
1976
31 JAN.
1978
13 FEB.
1981

Figure A4

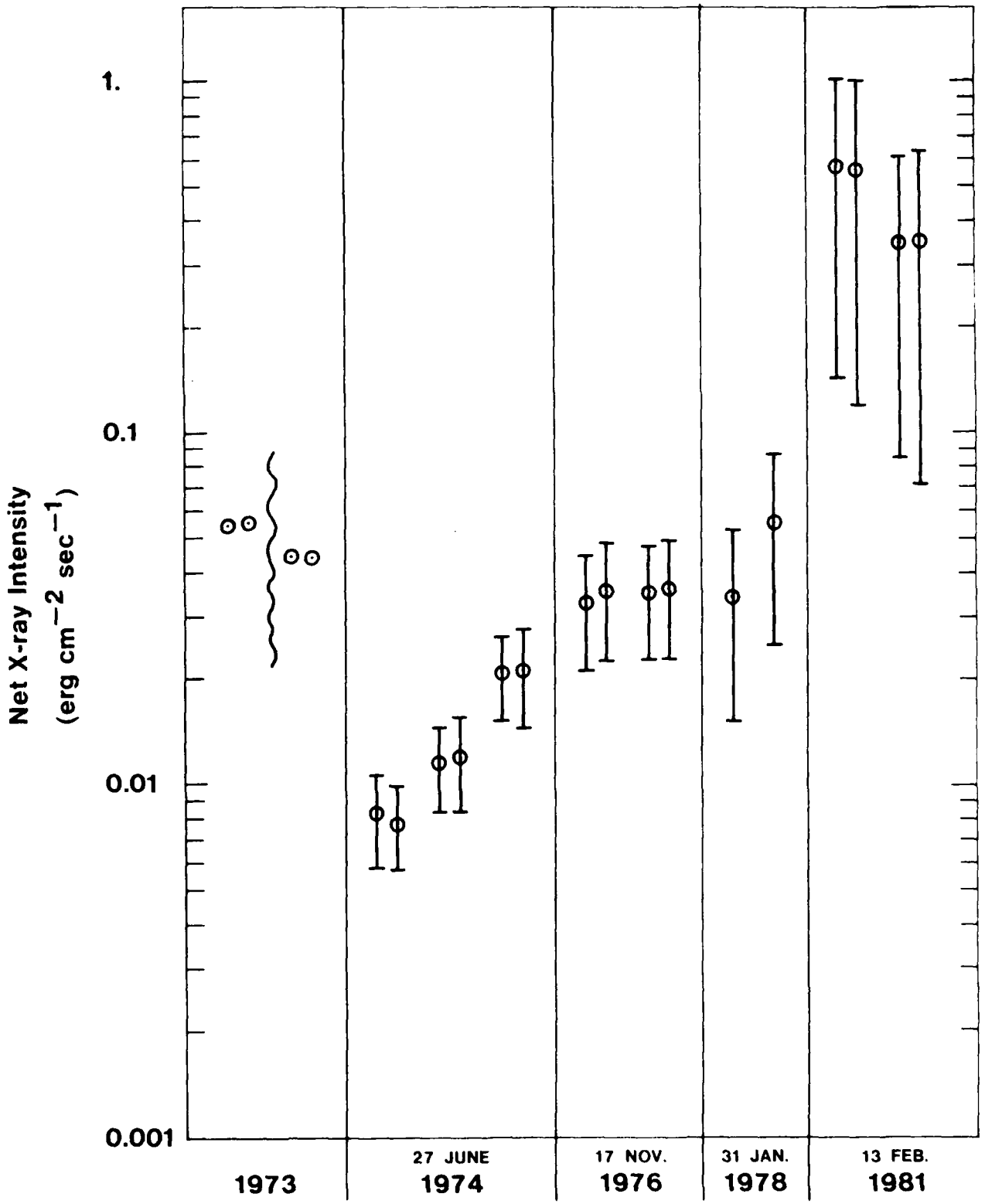
Net X-ray Intensity
(erg cm^{-2} sec^{-1})
1.
0.1
0.01
0.001
1973
27 JUNE
1974
17 NOV.
1976
31 JAN.
1978
13 FEB.
1981

Figure A5

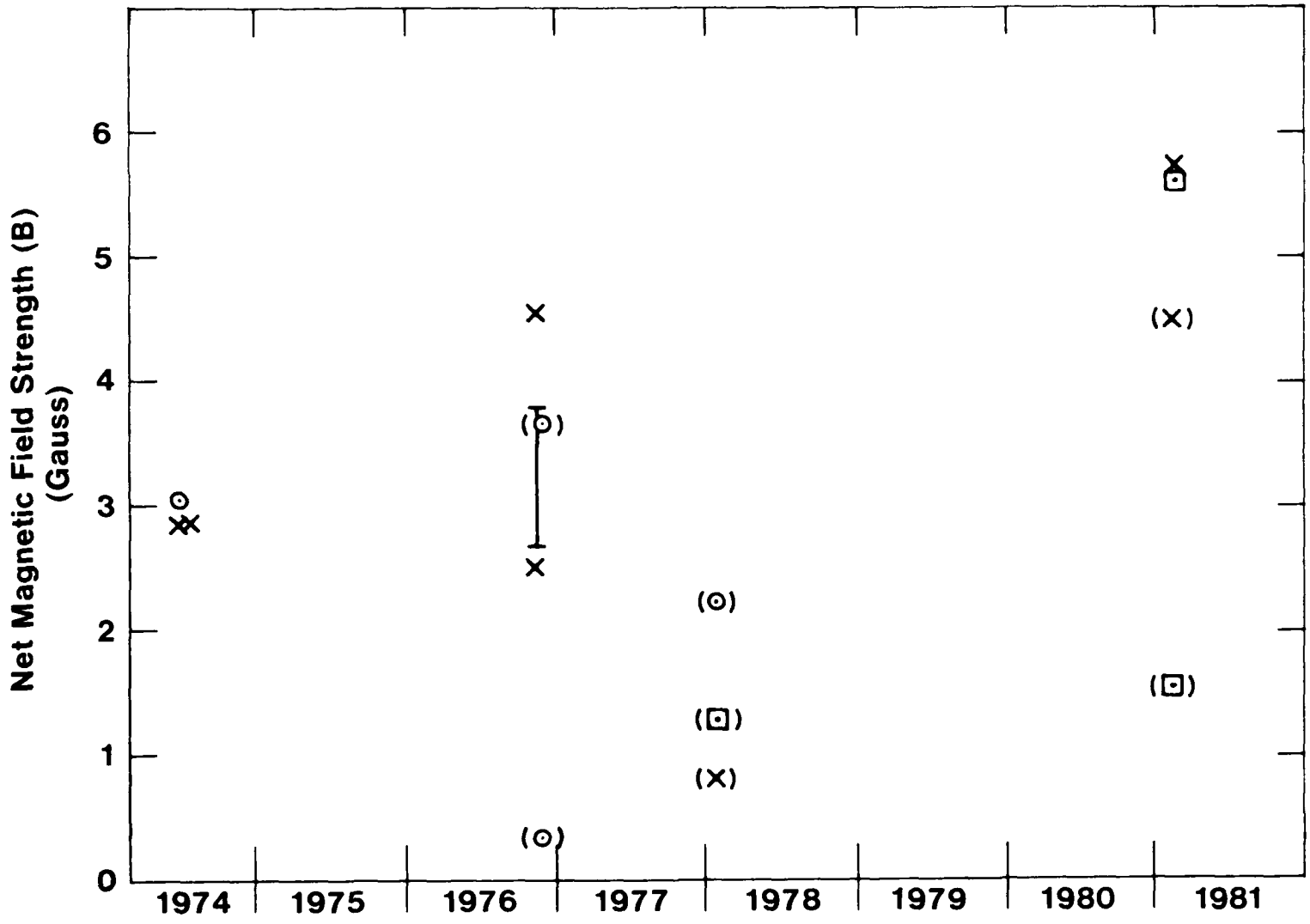
Net Magnetic Field Strength (B)
(Gauss)
0
1
2
3
4
5
6
1974
1975
1976
1977
1978
1979
1980
1981

Figure A6

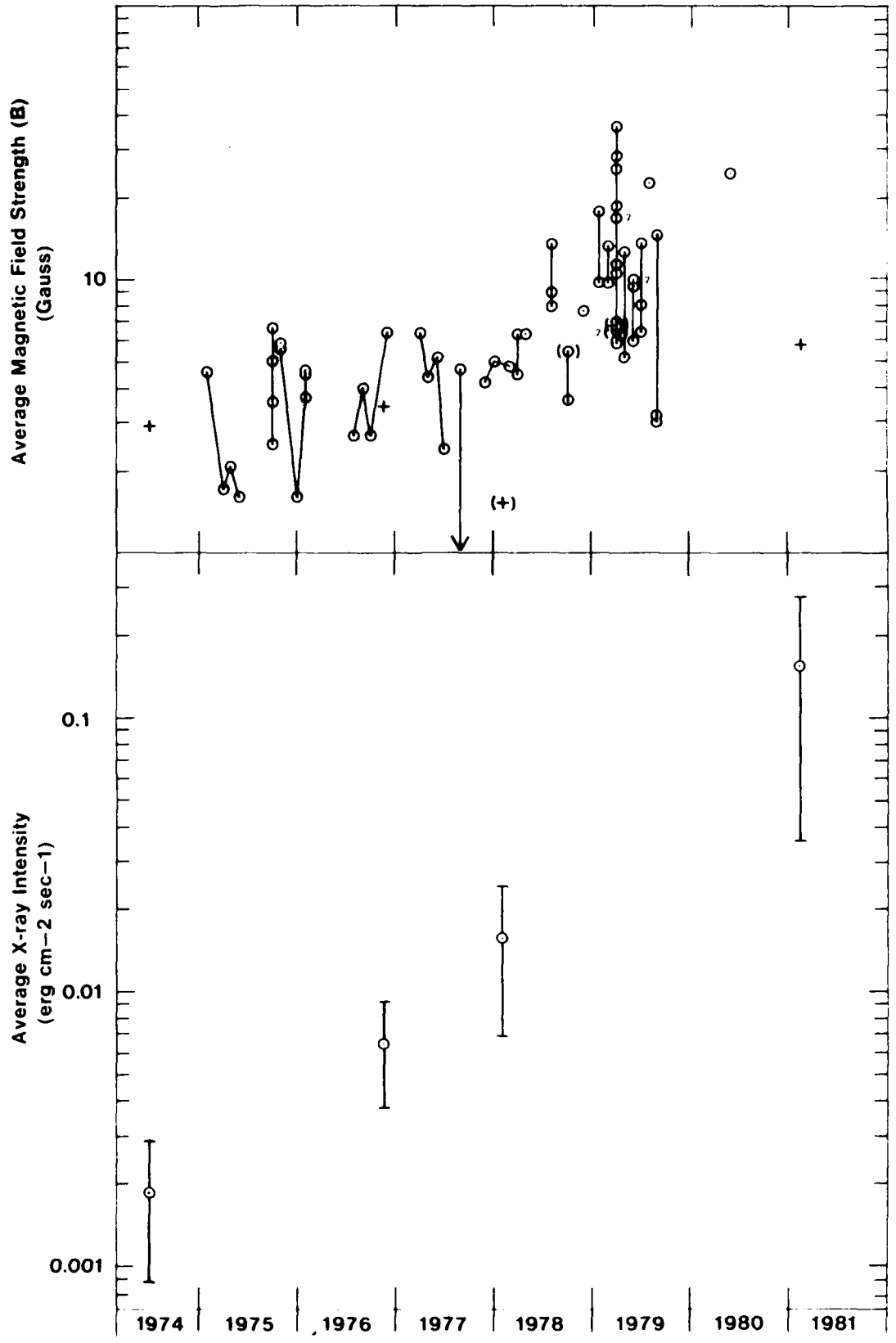
Average Magnetic Field Strength (B)
(Gauss)
10
(+)
Average X-ray Intensity
(erg cm−2 sec−1)
0.1
0.01
0.001
1974
1975
1976
1977
1978
1979
1980
1981

Figure A7

13 - 14 FEBRUARY 1981

AS&E X-RAY IMAGE

13, 1916 UT

KPNO MAGNETOGRAM

13, 1507 UT

MT. WILSON MAGNETOGRAM

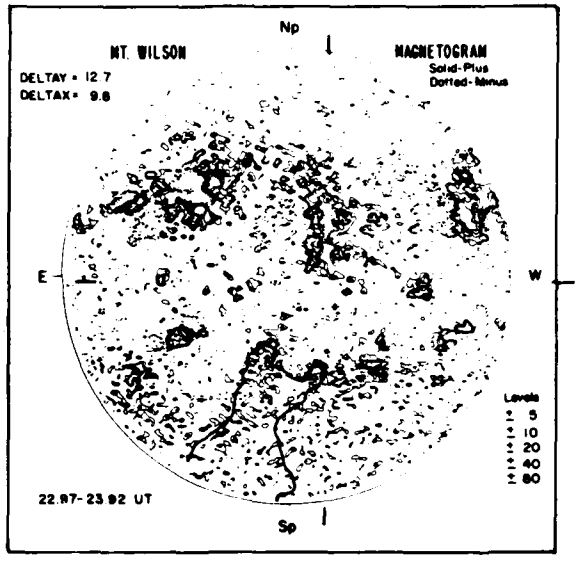

14, 2326 UT

Figure A8

SL-0821

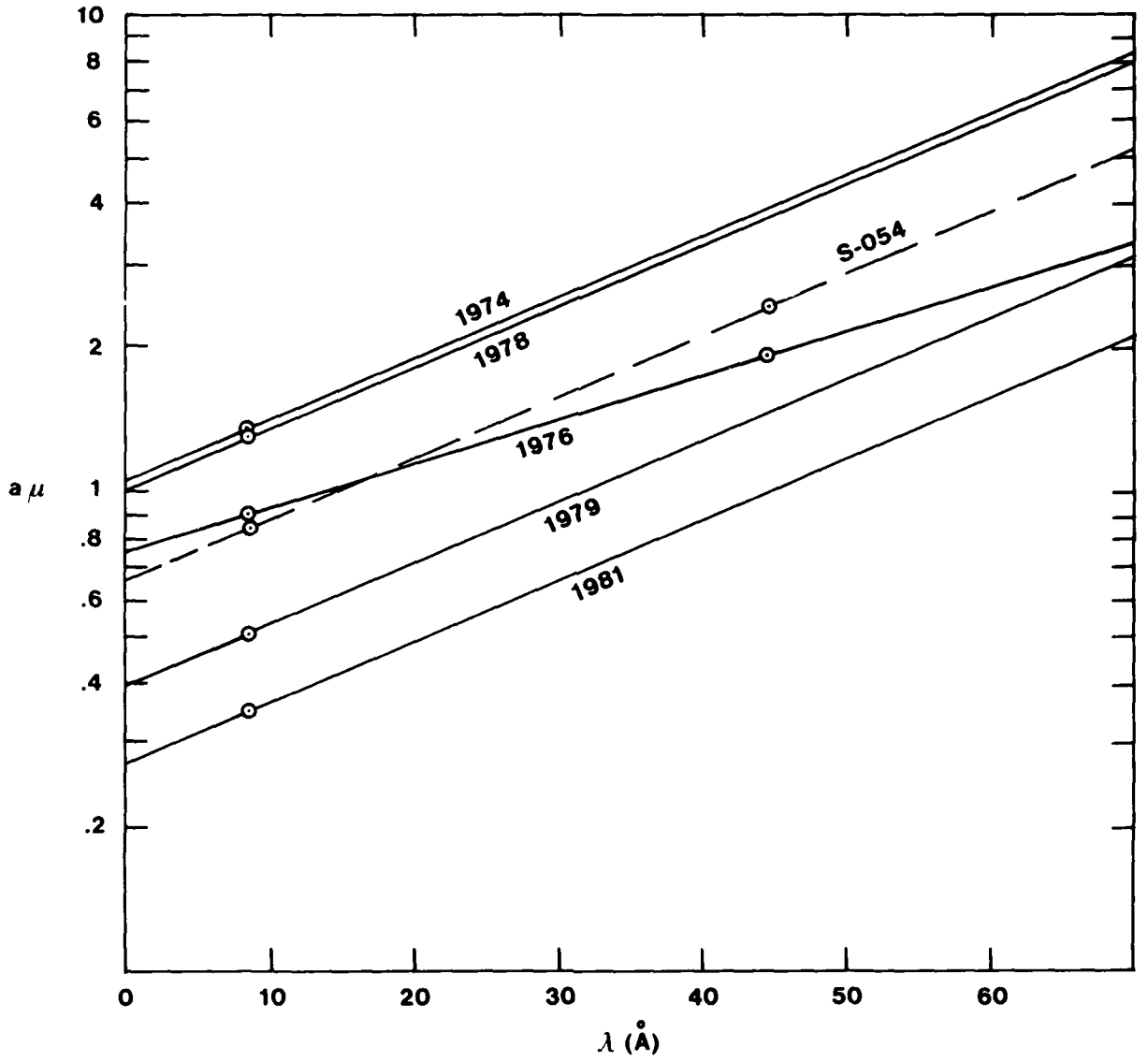
10
8
6
4
2
1
.8
.6
.4
.2
a μ
0
10
20
30
40
50
60
λ (Å)
1974
1978
S-054
1976
1979
1981

Figure A9

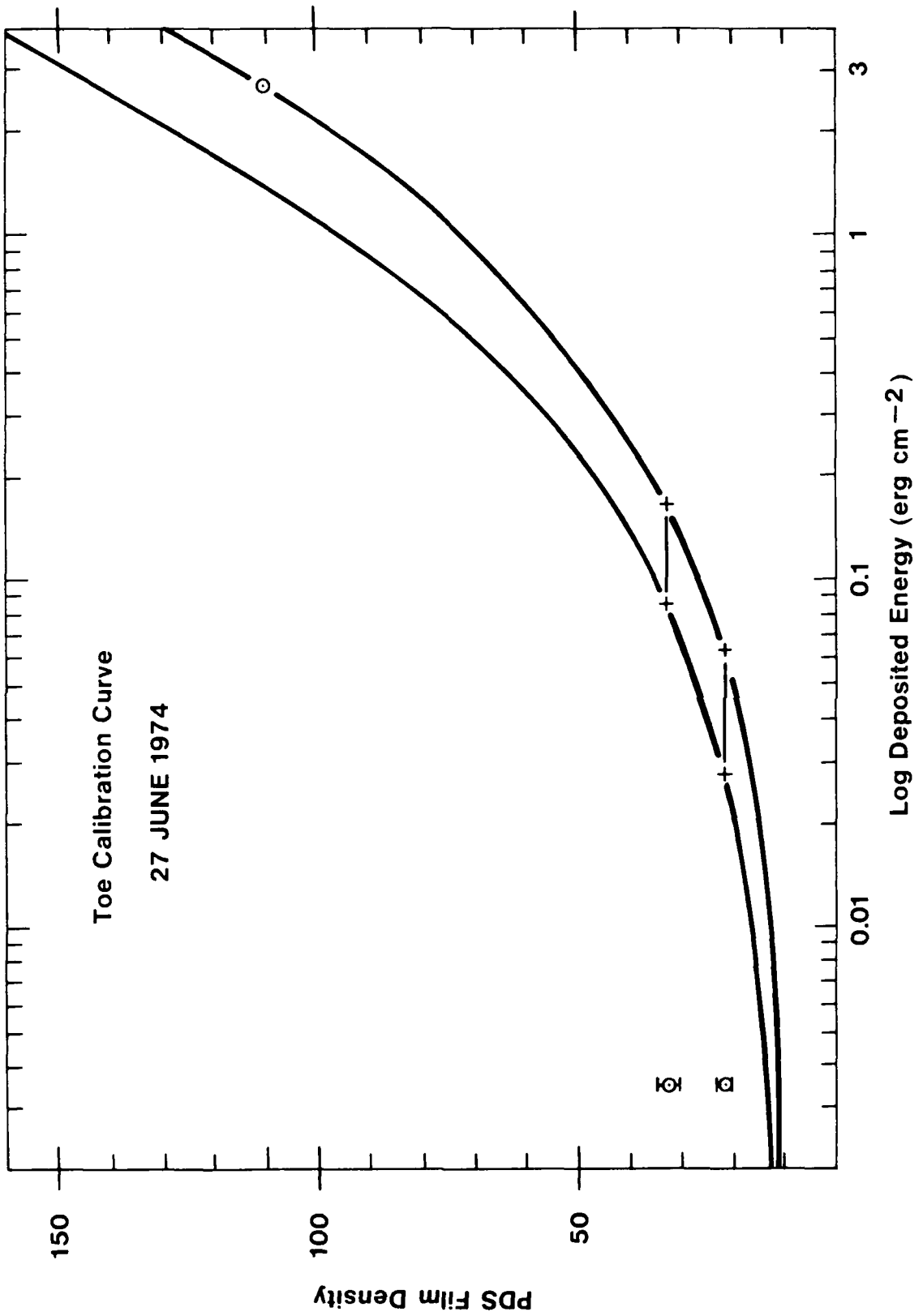
Toe Calibration Curve
27 JUNE 1974
PDS Film Density
150
100
50
Log Deposited Energy (erg cm−2)
0.01
0.1
1
3

Figure A10

END

FILMED

7-85

DTIC